OXFORD JOURNAL
OF STUDENT
SCHOLARSHIP

# Effect of Blade Length on Aerodynamic Power, Structural Loading and Cost of a Small Wind Turbine Rotor

Shravan Sajan
shravan.sajan@gmail.com

## ABSTRACT

Blade length is an important factor in preliminary rotor design, as it significantly affects aerodynamic energy capture, structural loading, and manufacturing considerations. To produce more power with a larger rotor, though, more torque is achieved at the same time as more thrust, bending loads, deformation, and production requirements. The effects of these couplings are explored in this study, with rotor blade lengths varying from 2.0 m to 8.0 m, to gain a better understanding of the aerodynamics and structure of a rotor blade as it scales up. Numerous models were implemented, such as an aerodynamic power model ( parametric model), Blade Element Momentum (BEM) analysis, BEM-coupled structural model, manufacturing cost model, and Monte Carlo uncertainty-propagation analysis. Both the BEM and the structural analyses have been done at 8 m/s, while the parametric model has been done at 12 m/s wind speed. The BEM model yielded an aerodynamic rotor power of 1.73 to 27.74 kW. A simplified Reynolds-independent airfoil polar yielded a maximum power coefficient of $C_{p,\,\max} = 0.440$ at an optimum tip-speed ratio of $\lambda = 2.9$, below the Betz limit of 0.593. Torque rose from 149 to 9,566 N·m and thrust rose from 384 to 6,137 N from the 2 m rotor to the 8 m rotor, with a corresponding increase in the flapwise root bending moment and tip deflection of about 64 times and 76 times, respectively, but the adopted screening criteria for stresses and deflections were not violated. Monte Carlo analysis resulted in a mean efficiency-adjusted parametric power of 81.3 kW with a 14.6 kW standard deviation, while deterministically, it was 80.4 kW. As a whole, the findings illustrate the impact of rotor size and aerodynamic and structural implications, and offer a first look at the rotor-scaling trade-offs.

***Keywords:*** wind turbine; blade length; rotor swept area; power coefficient ($C_p$); Betz limit; Blade Element Momentum (BEM); tip-speed ratio; aerodynamic drag; structural loading; Relative Manufacturing Cost Index; renewable energy

## 1. INTRODUCTION

Wind is an important renewable energy source for generating low-carbon electricity. Some of the energy of the moving air is transformed into rotational energy at the rotor blades of a wind turbine, and an

electricity-generating wind turbine converts some of this rotational energy into electrical energy in a generator. Although the direct operational emissions of wind turbines are very low, there are indirect emissions that are associated with the production of materials, manufacture of wind turbines, transportation, installation, and decommissioning of wind turbines (Alipour & Rahimpour, 2024). Thus, it is a non-polluting source of energy. It is of utmost importance that understanding of the relationship between turbine design and power generation is improved in order to improve the efficiency of wind-energy systems. There is already a formula to calculate the power produced by a wind turbine (Betz 1920, translated 2013; Okulov & van Kuik, 2009):

$$P = C_p \cdot (1/2) \cdot \rho \cdot A \cdot U^3 \qquad \textbf{(Equation 1)}$$

- $\rho$ = Density of air (1.225 kg/m³)
- A = Rotor swept area
- Cp = Power coefficient
- U = Wind speed

For an ideal actuator disc, the theoretical maximum power coefficient is the Betz limit, $C_{p,Betz} = 16/27 \approx 0.593$ (Betz 1920, translated 2013). In practice, the energy efficiency of the rotors is limited to values less than this ideal value due to aerodynamic losses and other non-ideal effects (Biswas and Chen 2025). So, the rotor swept area (which is proportional to the rotor blade length, the length of the rotor blades) plays a crucial role in the power of the wind turbine (Betz 1920, translated 2013).

$$A = \pi \cdot r^2 \qquad \textbf{(Equation 2)}$$

Where r = length of a rotor blade. The theoretical equation should show that the power should be proportional to the square of the rotor's length. Normal simplified equations, however, don't consider the mechanical or aerodynamic rotor power losses or the efficiency of the generator and the structural constraints.

The aerodynamic power, blade loadings, and mass are not the same for a rotor of any size and have been studied extensively in the case of rotor scaling. Canet, Bortolotti and Bottasso (2021) demonstrated that scaling a rotor is a multi-component phenomenon (Canet et al. 2021), as there are aerodynamic, elastic, inertial and gravitational effects which have to be considered simultaneously, and that not all the full-scale characteristics can be preserved by simple geometric scaling. Swept area R2 is approximately proportional to aerodynamic power capture, whereas other size-dependent structural quantities that depend on mass, volume, etc. of the blades have a higher size dependence. While this square–cube imbalance is the primary incentive to study rotor-size effects, practical rotor designs can differ significantly from the ideal geometric scaling in terms of material, structural architecture, airfoil geometry, and control strategy.

The aerodynamic power estimate was multiplied by an overall efficiency factor of $\eta = 0.90$ when using the simplified parametric calculation. This efficiency adjustment is for comparison purposes only and does not constitute an aerodynamic rotor power generator or power conversion model.

$$P_{adj} = 0.5\rho A U^3 C_p \eta \qquad \textbf{(Equation 3)}$$

General rotor-scaling laws have been developed in previous studies, and the aerodynamic optimization and structural design and wind-turbine cost scaling have been studied separately (Firoozi et al. 2024; Hu et al. 2013). A simplified comparative framework, however, that follows the same collection of geometrically scaled small-rotors in terms of aerodynamic performance, BEM-derived structural loading, and a transparent relative-cost model, is still useful in illustrating how these trends interact. The present study is then based on a corrected swept-area parametric model, a BEM aerodynamic model, and a directly coupled Euler–Bernoulli structural model with rotor radii ranging from 2 to 8 m. The goal is not to develop universal turbine scaling laws (Mehta et al. 2023), but to quantify the trends created by this defined simplified model and to determine where the model predictions match and/or diverge from published rotor-scaling trends. The key contribution is the internally consistent comparison of aerodynamic power, the blade loading derived from the BEM, structural response, and the relative manufacturing cost trends over the same range of rotor radius (2–8 m) and the explicit identification of limitations imposed by geometric similarity, Reynolds-invariant airfoil data, and simplified structural and cost formulations.

## 2. METHODOLOGY

### 2.1 Simulation Setup and Parameters

MATLAB was mainly used to perform primary parametric calculations. The rotor aerodynamics at the rotor level and the loading of each rotor section were assessed using the Blade Element Momentum (BEM) solver outlined in Section 2.3. The basic constants and the assumptions used in the structure are given below (Okulov and Sørensen 2008; Helge Aa. Madsen et al. 2009):

**Table 1**. Basic constants and assumptions used in the structure

| **Parameter** | **Value / Assumption** |
|---|---|
| Air density (ρ) | 1.225 kg/m³ |
| Wind speed (U) | 12 m/s (Primary Parametric) / 8 m/s (BEM analysis) |
| Power coefficient ($C_p$) | 0.42 (Parametric Baseline) |

| **Parameter** | **Value / Assumption** |
|---|---|
| Overall efficiency factor used in simplified parametric power estimate (η) | 0.90 |
| Oswald efficiency factor (e) | 0.88 |
| Fixed lift coefficient ($C_L$) | 0.8 |
| Young's modulus (E) | 35 GPa |
| Base chord length ($C_0$) | 0.30 m |
| Chord growth rate (k) | 0.04 m per metre of span |
| Blade root thickness base ($t_{root,\,0}$) | 0.12 m (grows by 0.01 m per metre of span) |
| Tip thickness ratio | 35% of root thickness |
| Wingspan range | 2.0 m to 8.0 m |
| Spanwise structural resolution | 200 points |

The value $C_p = 0.42$ is kept fixed for the simplified parametric power calculation as a baseline assumption, which is not output of the BEM solver. $C_{p,\,\max} = 0.440$ is predicted by the independently evaluated BEM model at $\lambda \approx 2.9$. The two values therefore correspond to different parts of the analysis: $C_p = 0.42$ is a prescribed parametric input, whereas $C_{p,\,\max} = 0.440$ is a BEM-predicted maximum.

**2.2 Aerodynamic Power Model**

The fundamental theory of wind energy says that the efficiency-adjusted parametric power estimate generated depends on the swept area ($A = \pi \cdot r^2$) of the rotating blades, which is the circular disc intercepted by the blades as they rotate (Burton et al. 2011). To test the loads on the structural beams while also considering the aerodynamics of the finite wings, the rotor design is tested with an equivalent wing planform model. The wind-power calculation was based on the rotor swept area,

$$A = \pi R^2, \qquad \textbf{(Equation 4)}$$

where $R$ is the blade length (rotor radius). The corresponding efficiency-adjusted parametric power estimate was calculated as

$$P_{adj} = \frac{1}{2}\rho\pi R^2 U^3 C_p \eta. \qquad \textbf{(Equation 5)}$$

Blade planform area was not used as the wind-energy capture area.

**2.3 Blade Element Momentum (BEM) Aerodynamic Analysis**

The aerodynamic behaviour at the rotor level reported in Section 3.7 and Table 3 was computed with the Blade Element Momentum (BEM) solver described below, which is part of the general BEM formulation presented by Manwell et al. (2009) and Le et al. (2025):

**2.3.1 Blade Geometry:** The blade geometry was defined by a design tip-speed ratio of $\lambda_{design} = 2.5$, a design lift coefficient of $C_l = 0.8$, and $B = 3$ blades. The design tip-speed ratio is a parameter for the geometry generation and was not used as the optimum operating condition. Following this, rotor performance was then tested under tip-speed-ratio conditions ranging from $\lambda = 1$–9, and the optimum operating point for maximum-$C_p$ was determined.

**2.3.2 Airfoil Aerodynamics:** Lift and drag vs. angle of attack is a linear pre-stall model (with lift-curve slope of 5.7 rad$^{-1}$ and zero-lift angle of -3° and stall at $C_{l,\,max}$ of 1.35), mixed with a Viterna-Corrigan-style flat-plate extrapolation for post-stall angles, a common approach in preliminary wind turbine BEM codes (e.g., NREL AeroDyn/CCBlade) rather than measured polar data for one named airfoil. This $-3^{\circ}$ zero-lift angle belongs specifically to the simplified polar used by the BEM solver.

**2.3.3 Induction Solution:** The blade was discretised with 24 spanwise BEM stations. The axial and tangential induction factors (a, a') were solved by iterative calculation at every operating point and each station (Andrew Ning 2013) based on Prandtl tip-loss correction and Glauert high-induction correction (Shen et al. 2005; Zhong et al. 2024). The results of the grid-convergence study outlined in Section 2.6 were used to evaluate the adequacy of the 24-station discretization.

**2.3.4 Performance Extraction:** The loads (dT, dQ) at each point around the blade span can be numerically integrated to get the thrust and torque, and the power is the product of torque and the blade's angular velocity (Ω). The operating point for each blade length is not assumed, but rather determined by performing a tip speed ratio sweep (1-9 λ) in each case to find the corresponding $C_{p,\,max}$. The sectional aerodynamic loads were also preserved to be included in the structural analysis, in addition to the quantities of the rotor performance which were integrated. At each radial station, the aerodynamic force was resolved into a component normal to the rotor plane, $dF_n$, and a tangential component, $dF_t$. These sectional forces were directly transferred to the structural model presented in Section 2.6. This means that, within the aerodynamic and structural analyses, the same BEM-derived spanwise loading is applied, instead of separate aerodynamic loads.

**2.4 Induced Drag and Power Loss**

The blade aspect ratio was defined as

$$AR = \frac{b^2}{S}, \qquad \textbf{(Equation 6)}$$

where $b$ is the blade span and $S$ is the blade planform area. The Oswald efficiency factor is denoted by $e$. Finite-wing theory was used to calculate the induced drag. CDi was calculated as follows (Manwell et al. 2009) :

$$C_{D,i} = C_L^2 / (\pi \cdot e \cdot AR) \qquad \textbf{(Equation 7)}$$

Induced drag force Di, as well as power loss ($P_{loss}$), was estimated with the dynamic pressure, where $q = \frac{1}{2}\rho U^2$ is the dynamic pressure.

$$Di = q \cdot S \cdot C_{D,i} \qquad P_{loss} = Di \cdot U \qquad \textbf{(Equation 8)}$$

**2.5 Required Angle of Attack**

The finite-wing lift slope a_finite was calculated based on the 2D lift slope $a_0 = 2 \cdot \pi$:

$$a_{finite} = a_0 / (1 + (a_0 / (\pi \cdot e \cdot AR))) \qquad \textbf{(Equation 9)}$$

For consistency with the simplified aerodynamic polar used in the BEM analysis, the zero-lift angle was taken as $\alpha_{L0} = -3^{\circ}$. The required angle of attack for the target lift coefficient was then calculated as:

$$a_{required} = (C_L / a_{finite}) + \alpha_{L0} \qquad \textbf{(Equation 10)}$$

**2.6 Structural Analysis Using BEM-Derived Loads**

The structural analysis was modified, and the aerodynamic loads on each of the blades were directly calculated from the BEM model described in section 2.3. This elliptical lift distribution, which had been prescribed independently, was thus eliminated. The structural analysis was carried out for each rotor radius, with the loads in the radial (sectional) and tangential (tangential) directions at the operating point where the maximum power coefficient, Cp, was obtained. The BEM model is used to compute the sectional normal force (dFn) and the sectional tangential force (dFt) for each radial station. The normal force was considered the aerodynamic flapwise loading, and the tangential force was considered the aerodynamic edgewise loading. Aerodynamic moments corresponding to each one of the blades were obtained by numerical integration of the sectional forces on the blade span.

$$M_{flap} = \int r dF_n \qquad \textbf{(Equation 11)} \quad \text{and}$$

$$M_{edge} = \int r dF_t. \qquad \textbf{(Equation 12)}$$

Since the aerodynamic part of the blade starts at the modelled hub radius, moments about the rotor axis were separated from the moments at the blade clamp. The moments of structure root bending moments reported in this study are, thus, moments at the blade-modeled clamp.

Aerodynamic stations were chosen for calculation of sectional BEMs and then interpolated to the existing structural grid of 200 points. To ensure that the sectional forces were correct, the forces were integrated again to calculate the BEM rotor thrust and torque, and it matched numerically with the original values. The loads were then interpolated onto the structural grid, and the difference between the integrated loads and the BEM loads was about 0.74% for thrust and 0.45% for torque.

The blade was represented as an Euler–Bernoulli beam (Öchsner 2021) with Young's modulus E=35 GPa. The current simplified section property model that is dependent on chord and thickness was preserved. Distributed loads were computed from the BEM, and the spanwise internal flapwise and edgewise bending moments were calculated. Combined flapwise and edgewise bending stresses were used to determine maximum bending stress, and the Euler–Bernoulli curvature was integrated along the blade (flapwise) to determine tip deflection.

Gravitational and centrifugal loads were not accounted for, as the simplified blade model did not have the validated spanwise blade-mass distribution. The results in this paper are therefore aerodynamic loadings at the selected steady BEM operating condition and not full turbine design loadings. The present analysis does not take account of transient gust, gravitational, centrifugal, and aeroelastic loads.

### 2.6.1 Structural Utilization Criteria

To determine whether the predicted structural response approached a defined limit within the investigated rotor-radius range, stress and deflection utilization ratios were calculated. Stress utilization was defined as

$$U_\sigma = \frac{\sigma_{max}}{\sigma_{allow}}, \qquad \textbf{(Equation 13)}$$

where $\sigma_{max}$ is the maximum combined bending stress and $\sigma_{allow}$ is the stated material allowable. Deflection utilization was defined as

$$U_\delta = \frac{\delta_{tip}}{\delta_{allow}}, \qquad \textbf{(Equation 14)}$$

where $\delta_{tip}$ is the calculated flapwise tip deflection and $\delta_{allow}$ is the stated blade-clearance screening criterion. A utilization ratio of 1.0 represents the adopted limit for the corresponding criterion. Values below 1.0 indicate that the criterion is not reached.

For the present simplified analysis, a stress allowable of $\sigma_{allow} = 100$ MPa was adopted as a conservative screening criterion. The allowable flapwise tip deflection was defined as $\delta_{allow} = 0.10R$. Stress and deflection utilization were therefore calculated as

$$U_{\sigma} = \frac{\sigma_{max}}{100\ MPa} \qquad \textbf{(Equation 15)}$$ and

$$U_{\delta} = \frac{\delta_{tip}}{0.10R}. \qquad \textbf{(Equation 16)}$$

A utilization ratio of 1.0 represents the adopted screening limit.

### 2.6.2 Numerical Convergence Assessment

The aerodynamic and structural discretizations were checked for convergence by a numerical convergence study. In the case of the BEM model, more and more spanwise stations were added, and the maximum power coefficient, thrust, and torque were compared to a reference solution with a finer grid. In order to assess the structural model, the number of beam points was increased in a progressive manner, and the flapwise root bending moment, the maximum stress, and tip deflection were compared to a reference solution obtained on a finer grid. The production discretizations of 24 BEM stations and 200 structural points were kept since the output quantities changed in a relatively small amount when further grid refinement was conducted.

## 2.7 Relative Manufacturing Cost Index Model

Relative Manufacturing Cost Index was estimated across three scaled variables:

$$C_{total} = C_{material} + C_{reinforcement} + C_{fabrication} \qquad \textbf{(Equation 17)}$$

Material cost: Directly proportional to the volume of the blades (Average thickness × area at 5000 units/m³).

Reinforcement cost: Proportional to root bending moment (scaling factor 0.015).

Fabrication cost: Proportional to blade span and chord (scaling factor 120).

## 2.8 Monte Carlo Uncertainty Propagation

A Monte Carlo uncertainty-propagation analysis was used to estimate the sensitivity of the simplified parametric power model to the prescribed wind-speed variability. The samples are synthetic and are not experimental or numerical simulations independent of the deterministic samples. The wind speed at each radius of the rotor was sampled from a normal distribution,

$$U_s \sim \mathcal{N}(U_0, (0.06\,U_0)^2) \qquad \textbf{(Equation 18)}$$

where the nominal wind speed was $U_0 = 12$ m/s, and the standard deviation was $0.72$ m/s, corresponding to a prescribed turbulence intensity of 6%. To ensure reproducibility, a fixed MATLAB random-number seed of 1, based on the Mersenne Twister random-number generator, was used.

For each realization, the wind speed sampled was used in the deterministic efficiency-adjusted parametric power equation. The electrical/generator noise, CFD uncertainty, perturbation of the structural properties, and repeated application of the wind-speed perturbation were not included. The Monte Carlo results are reported in terms of the sample mean and sample standard deviation, and are only interpreted as a representation of uncertainty propagation when the wind speed distribution is prescribed.

### 2.9 BEM Verification Case

The BEM implementation was also compared with controlled, NASA Ames wind tunnel measurements of the published NREL Phase VI Unsteady Aerodynamics Experiment rotor. The Phase VI configuration features two 10.06 m-diameter S809 airfoil blades rotating at about 72 rpm. The published rotor geometry, operating conditions, and aerodynamic data were used to construct a separate verification case. The predicted rotor performance was then compared with that which is published. There was no attempt to scale up the geometrically scaled rotors (2–8 m) used in the main parametric study for this verification case, and it was only used for assessing the implementation of the BEM methodology.

## 3. RESULTS

### 3.1 Parametric simulation of the 2.0–8.0 m span range

The output of the parametric model is shown here over the entire range of blade lengths at a constant wind speed of 12 m/s. The BEM-coupled structural responses across the investigated rotor-radius range are summarized in Table 2.

**Table 2**: Structural response calculated using BEM-derived aerodynamic loading at the maximum-$C_p$ operating point.

| R (m) | Mflap (N·m) | Medge (N·m) | Stress (MPa) | Tip defl. (mm) | $U_\sigma$ | $U_\delta$ |
|---|---|---|---|---|---|---|
| 2 | 139 | 40 | 0.184 | 0.093 | 0.00184 | 0.00047 |
| 3 | 471 | 137 | 0.348 | 0.369 | 0.00348 | 0.00123 |

| | | | | | | |
|---|---|---|---|---|---|---|
| 4 | 1,116 | 324 | 0.530 | 0.935 | 0.00530 | 0.00234 |
| 5 | 2,179 | 632 | 0.718 | 1.856 | 0.00718 | 0.00371 |
| 6 | 3,766 | 1,092 | 0.907 | 3.171 | 0.00907 | 0.00529 |
| 7 | 5,980 | 1,735 | 1.091 | 4.898 | 0.01091 | 0.00700 |
| 8 | 8,927 | 2,589 | 1.270 | 7.039 | 0.01270 | 0.00880 |

The computed quantities increase as the rotor radius increases, but the rates of increase vary as a result of different model relationships. The corrected parametric power model shows that efficiency-adjusted power is directly proportional to the rotor swept area, $A = \pi R^2$, when wind speed, $C_p$, and η are held constant. The quadratic dependence of power on rotor radius is therefore imposed by the governing equation, and is therefore not considered as an independent validation of the model.

### 3.2 Parametric Power and Monte Carlo Wind-Speed Uncertainty

The corrected deterministic parametric power calculation and the propagation of the prescribed 6% wind-speed variability are examined over the investigated rotor-radius range.

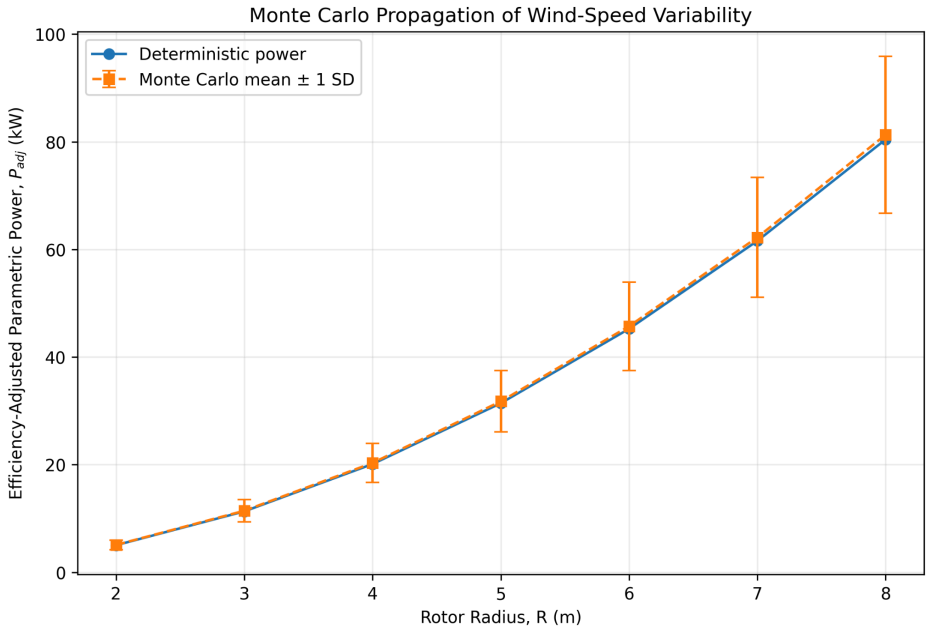



**Figure 1.** Propagation of prescribed wind speed variability using the parametric power model with efficiency correction through the Monte Carlo simulation. The deterministic power is indicated with circle markers, and the Monte Carlo mean with square markers with ±1 standard deviation error bars. The analysis used 100,000 normally distributed wind-speed samples with $U_0 = 12$ m/s and $\sigma_U = 0.72$ m/s. The Monte Carlo samples represent uncertainty propagation rather than experimental repeatability.

The Monte Carlo analysis yielded the anticipated propagation of wind-speed variability as a result of the cubic power relationship. The deterministic efficiency-adjusted parametric power estimate was 80.4399 kW, and the Monte Carlo mean power was 81.2985 kW with a standard deviation of 14.5911 kW for R=8 m. The mean relative increase in the Monte Carlo simulation compared to the deterministic simulation was 1.067%. For a zero-mean normally distributed wind-speed perturbation and $P \propto U^3$, the expected mean-power factor is

$$\frac{E[P]}{P(U_0)} = 1 + 3(0.06)^2 = 1.0108. \qquad \textbf{(Equation 19)}$$

The mean of the analytical result at R=8 m is found to be 81.3086 kW with a relative increase of 1.080% compared with the deterministic result. The Monte Carlo result thus closely matches the analytical prediction. Propagation of prescribed wind-speed uncertainty is indicated by the scatter in Figure 1, and is not to be equated with experimental repeatability.

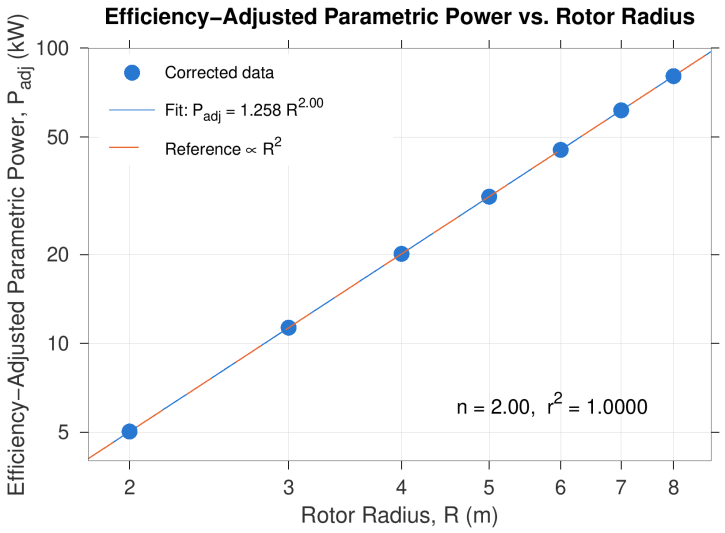



**Figure 2**. Log-log plot of mean simulated power against blade length, with a reference P ∝ r² slope. The fitted parametric exponent is n = 2.

Figure 2 is a re-plot of the same data on a log-log plot, allowing for the reading of the gradient as the scaling exponent. The fitted scaling exponent is $n = 2.00$, consistent with the theoretical $R^2$ dependence of rotor swept area. Because $A = \pi R^2$, the corrected parametric power estimate follows $P_{adj} \propto R^2$ when wind speed, $C_p$, and η are held constant.

### 3.3 Analysis of Induced Drag and Power Loss vs Blade Length

The aerodynamic drag and the power loss due to aerodynamic drag, computed from Equations 6 and 7, are the second parameter examined.

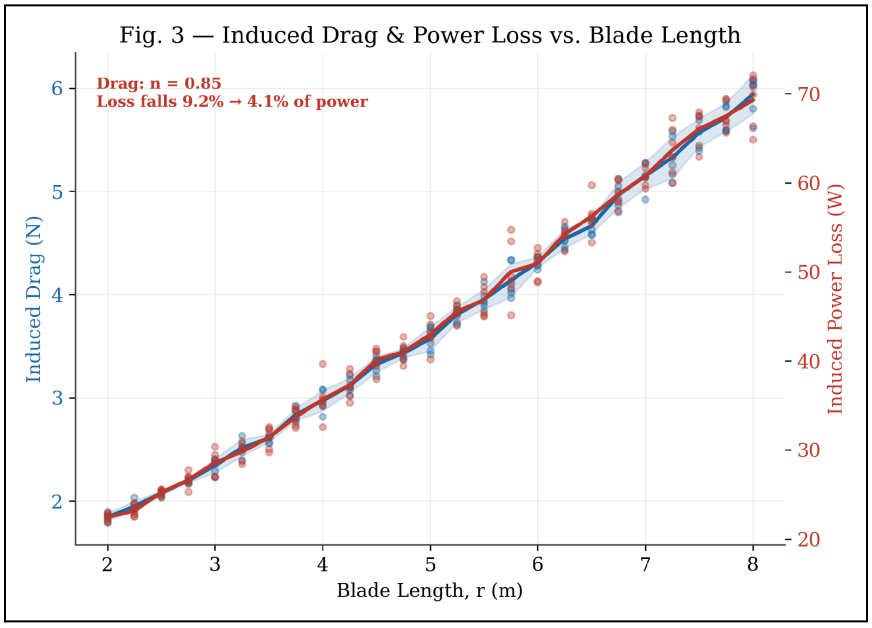



**Figure 3.** Induced aerodynamic drag and induced power loss as functions of blade length.

In both cases, as shown in Figure 3, induced drag is increased from 1.84 N to 5.95 N (3.2 times) and induced power loss from 22.1 W to 71.5 W (3.2 times). The fitted exponent is n = 0.85, which is much less steep than the exponent of power, n = 2. In the present simplified model, the induced drag increases as the rotor size increases, but the induced drag fraction decreases, since an increase in aspect ratio will decrease the induced drag coefficient. These results should be considered only under the assumptions of the finite wing model and are not to be interpreted as a practical limitation for the rotor size. This is because the coefficient of induced drag (aspect ratio) decreases with increasing aspect ratio (span). The induced-drag values calculated grow in magnitude as a function of blade length, and the relative contribution of induced-drag is in accordance with the finite-wing relationship presented above (Manwell et al., 2009; Kelele et al., 2022). .

### 3.4 Analysis of Required Angle of Attack vs Aspect Ratio

An important consideration with the drag behaviour is that the blade is required to work at a certain angle of attack in order to create the desired lift coefficient, as determined by Equations 8 and 9.

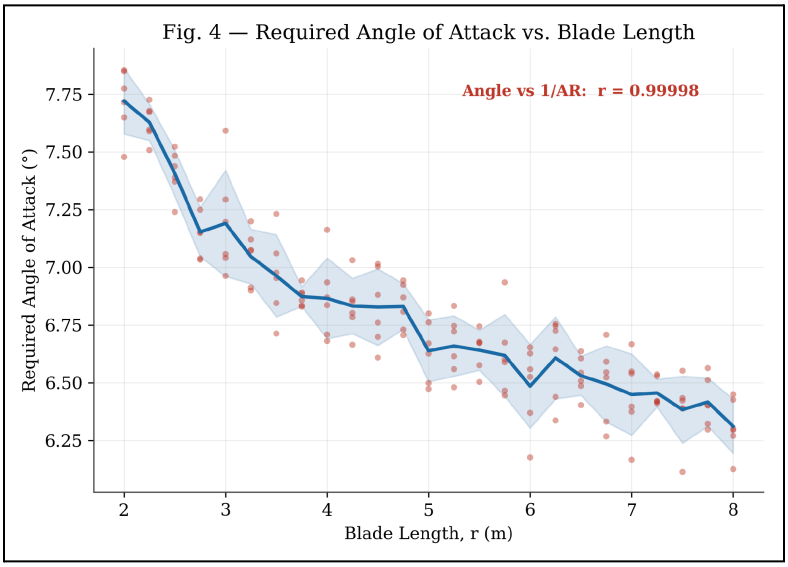



**Figure 4**. Required angle of attack decreases as aspect ratio increases with blade length, reducing flow-separation risk.

As aspect ratio increases from 6.67 to 14.81, the required angle of attack decreases from 7.78° to 6.41° in Figure 4. The relationship is almost perfectly linear over the range of the inverse of the aspect ratio (r = 0.99998), and is directly related to the finite-wing lift-slope formulation in Equation 8, which has an induced angle correction that is proportional to 1/AR. In terms of operation, it is desirable because the higher aspect ratio blades operate further away from stall, thus making it easier to avoid flow separation when gusty. This result, together with the trends of induced drag discussed in Section 3.3, demonstrates the variation of the aerodynamic quantities with aspect ratio in the simplified model used in this analysis.

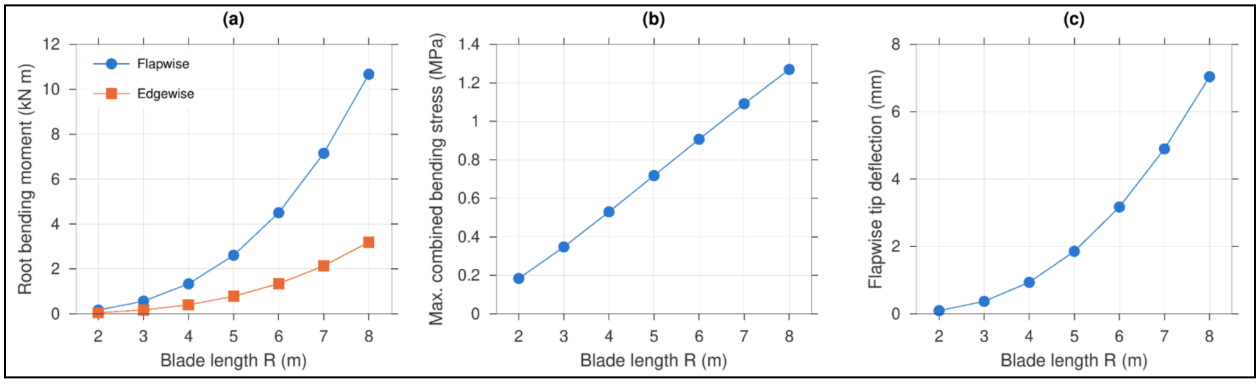
### 3.5 Structural Response Under BEM-Derived Aerodynamic Loading

The flapwise root bending moment was found for this BEM-coupled structural analysis to change from 139 N·m at R=2 m to 8,927 N·m at R=8 m, which is a factor of ~64.2. The flapwise tip deflection increased from 0.093 mm to 7.039 mm over the same distance, which is an order of magnitude of about 75.7 times. The aerodynamic edgewise root moment rose a dramatic 2,589 N·m from 40 N·m.

The increased aerodynamic force with rotor size and the increased moment arm about which this force acts both contribute to the substantially larger flapwise moment. Although the edgewise moment was smaller than the flapwise moment for all of the rotor sizes, it was still significant and was included in the combined stress calculation. The bending stress increased from 0.184MPa for the 2 m blade to 1.270MPa for the 8 m blade. The tip deflection of the flapwise change from 0.093 mm to 7.039 mm over the same range. The values are significantly higher than those found in the previous independently prescribed loading model, showing the significance of the use of an aerodynamic load distribution corresponding to the rotor-performance calculation.

The structural response was predicted and compared to the stated utilization criteria to determine if these responses are indicative of a structural limit within the range being investigated. The utilization ratio, in either case, was far from unity for the range of 2–8 m radius. The maximum bending stress and tip deflection of flapwise were obtained at R=8 m for both cases of calculation, namely 1.270 MPa and 7.039 mm, respectively. The utilization ratios are U=0.0127 and U=0.00880, respectively. Thus, for the steady aerodynamic loading considered in the present model, no stress limit or deflection limit for the structure of the blades was found in the range of blade lengths investigated. The results must be considered as a simplified steady aerodynamic structural response and should not be regarded as design-load predictions. The present beam model in the current study does not include gravity, centrifugal loading, transient gust loading, fatigue, material anisotropy, and aeroelastic deformation (Cardoza and Ning 2026; Ingersoll and Ning 2020).

**Figure 5.** Structural response under BEM-derived aerodynamic loading.




The BEM-derived structural responses are shown in Figure 5: (a) Flapwise and edgewise bending moments evaluated at the structural blade clamp; 5(b) maximum combined bending stress; and 5(c) flapwise tip deflection. At the maximum-Cp operating point, the BEM solution was computed, and the aerodynamic forces were interpolated onto the 200-point structural grid to be used as sectional aerodynamic forces. Gravity loading and centrifugal loading are not considered.

### 3.6 Analysis of Relative Manufacturing Cost Index vs Power Output

The modeled Relative Manufacturing Cost Index has an explicit term in it that is proportional to root bending moment. As a result, any correlation between modeled cost and root bending moment is a statistical correlation rather than an independent physical correlation, and is only a partial correlation.

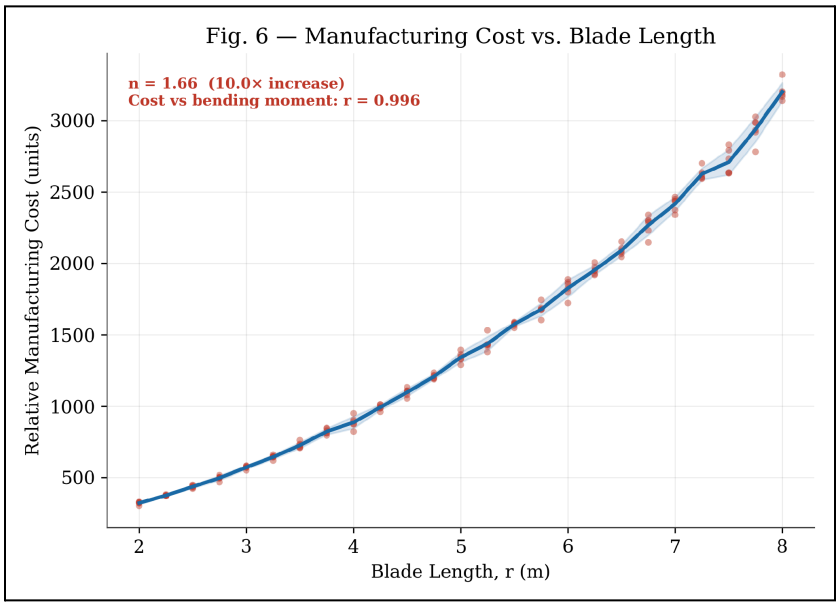



**Figure 6**. Modeled Relative Manufacturing Cost Index as a function of rotor radius, based on the prescribed material, reinforcement, and fabrication cost terms.

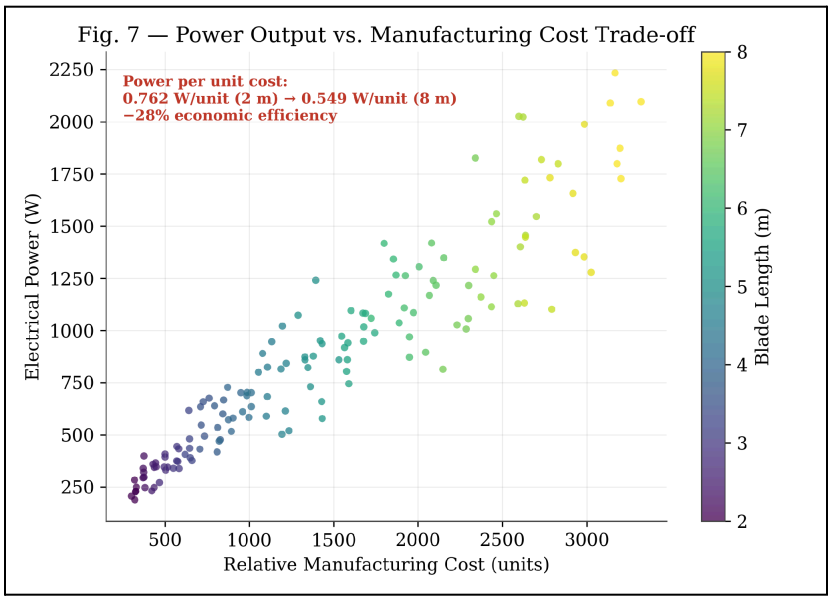



**Figure 7.** Corrected deterministic parametric power estimate versus modeled Relative Manufacturing Cost Index across the investigated rotor-radius range.

It is observed that the Relative Manufacturing Cost Index increases as power to the n = 1.66; it increases 10-fold from 314.7 to 3,146.7 units and correlates strongly with root bending moment (r = 0.996); this confirms that cost increases are due to root reinforcement rather than raw material volume, as seen in

Figure 6. This trade-off is expressed in Figure 7. Modeled Relative Manufacturing Cost increases with rotor radius, due to the presence of the radius-dependent material and fabrication components in the cost formulation as well as the explicit reinforcement term that is proportional to root bending moment. Thus, the relationship between power, structural loading, and the cost engendered is a result of the set of model equations that were prescribed and should be viewed descriptively and not as a separate, observed statistical correlation.

### 3.7 BEM rotor performance across blade lengths

The outcomes of the Blade Element Momentum model described in Section 2.3 are presented in this subsection. The BEM formulation is based on a swept rotor disc to evaluate rotor aerodynamic performance. The performance has been reported for each rotor at its optimum operating point, that is, by sweeping tip-speed ratio, λ = 1 to 9 and not by fixing it at a particular value.

**Table 3**: BEM-predicted aerodynamic rotor performance at $U = 8$ m/s. Power values represent aerodynamic rotor power calculated as $P_{aero} = Q\Omega$; no generator or electrical-conversion efficiency is applied.

| **R (m)** | **Optimal TSR** | **Cp, max** | **Thrust (N)** | **Torque (N·m)** | Aerodynamic rotor power, $P_{aero}$ (kW) |
|---|---|---|---|---|---|
| 2 | 2.9 | 0.440 | 384 | 149 | 1.73 |
| 3 | 2.9 | 0.440 | 863 | 504 | 3.90 |
| 4 | 2.9 | 0.440 | 1,534 | 1,196 | 6.94 |
| 5 | 2.9 | 0.440 | 2,397 | 2,336 | 10.84 |
| 6 | 2.9 | 0.440 | 3,452 | 4,036 | 15.61 |
| 7 | 2.9 | 0.440 | 4,698 | 6,409 | 21.24 |
| 8 | 2.9 | 0.440 | 6,137 | 9,566 | 27.74 |

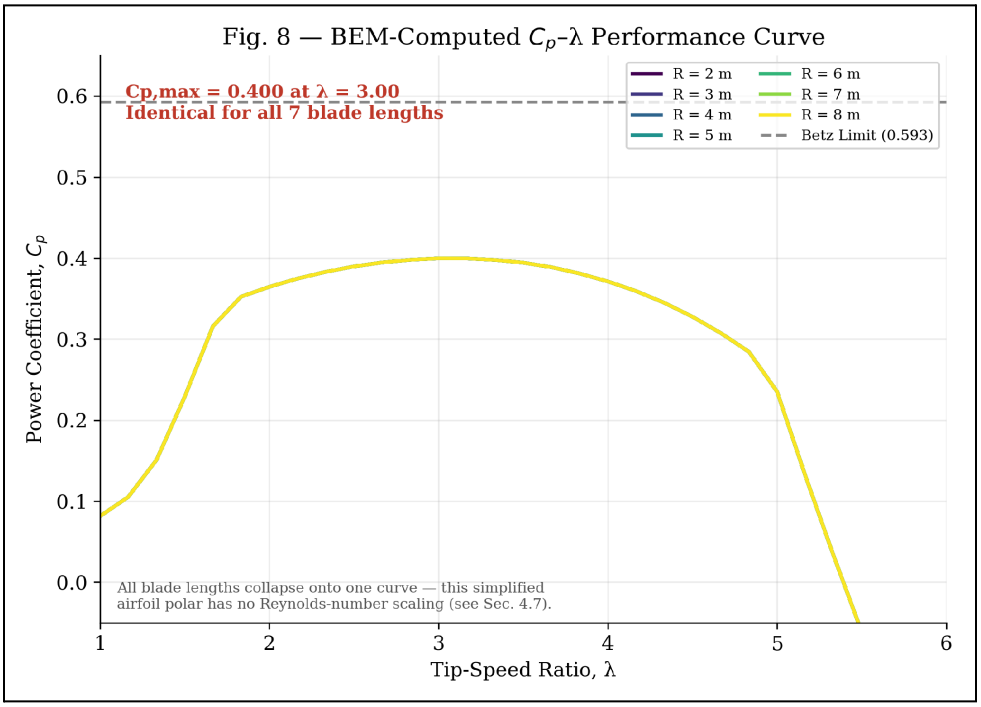



**Figure 8**. BEM-computed Cp–λ performance curve.

Figure 8 shows all seven blade lengths collapse onto a single curve peaking at $C_{p,\max} \approx 0.440$ near $\lambda = 2.9$, below the Betz limit of 0.593.

The BEM calculations produced coincident $C_p - \lambda$ curves for the geometrically scaled rotors, with a maximum power coefficient of approximately $C_{p,\max} = 0.440$ at a tip-speed ratio of approximately $\lambda = 2.9$. The coincident curves are due to the geometric similarity of the scaled rotor models and the Reynolds-independent aerodynamic polar employed in the present BEM formulation. As a result, the model cannot predict changes in aerodynamic efficiency that depend on rotor size and Reynolds number. This scale invariance is not an indication that real turbines of different sizes would have the same aerodynamic performance.

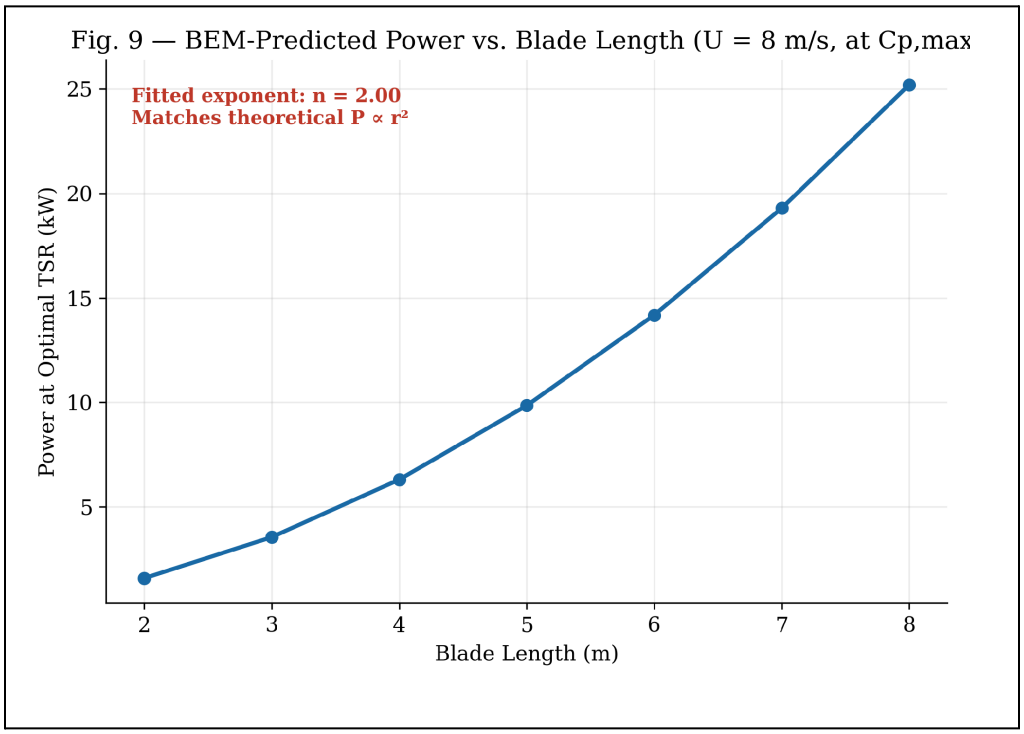



**Figure 9.** BEM-predicted aerodynamic rotor power as a function of rotor radius at $U = 8$ m/s. Figure 9 shows that the reported power is calculated from aerodynamic torque as $P_{aero} = Q\Omega$ and does not include generator or electrical-conversion losses.

At a wind speed of 8 m/s, the BEM-predicted aerodynamic power increased from approximately 1.73 kW for the 2 m rotor to 27.74 kW for the 8 m rotor. The corrected efficiency-adjusted parametric power estimate increased from approximately 5.03 kW at $R = 2$ m to 80.42 kW at $R = 8$ m. Because rotor swept area scales as $R^2$, the calculated power increased by a factor of 16 over this fourfold increase in rotor radius. The rotors are geometrically scaled, and due to the BEM model predicting an essentially constant maximum power coefficient of 0.440, power is expected to scale with the swept-area scaling, $P \propto r^2$. Increasing rotor radius by a factor of four therefore increased aerodynamic power by approximately a factor of sixteen.

### 3.8 Analysis of Torque, Thrust and Rotor Speed vs Blade Length

Next, the mechanical stresses and rotational speeds associated with the power gains in Section 3.7 are discussed.

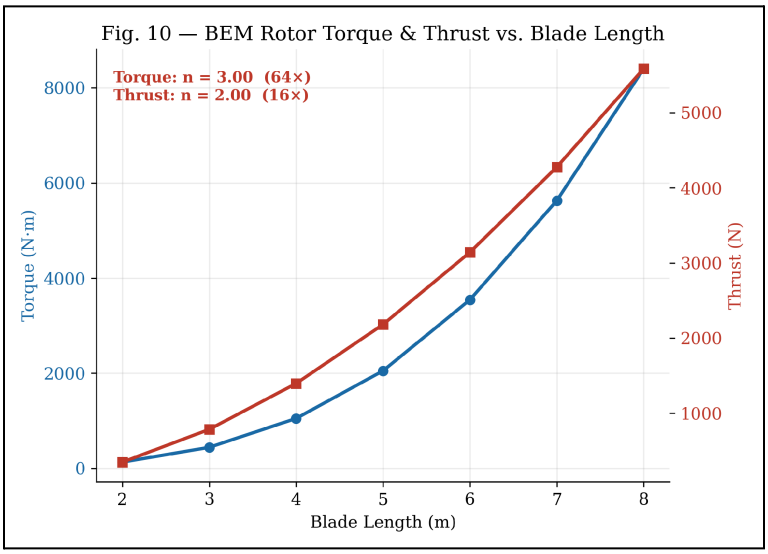



**Figure 10**. Rotor torque and thrust loading both increase sharply with blade length, driving the structural penalties in Figure 5.

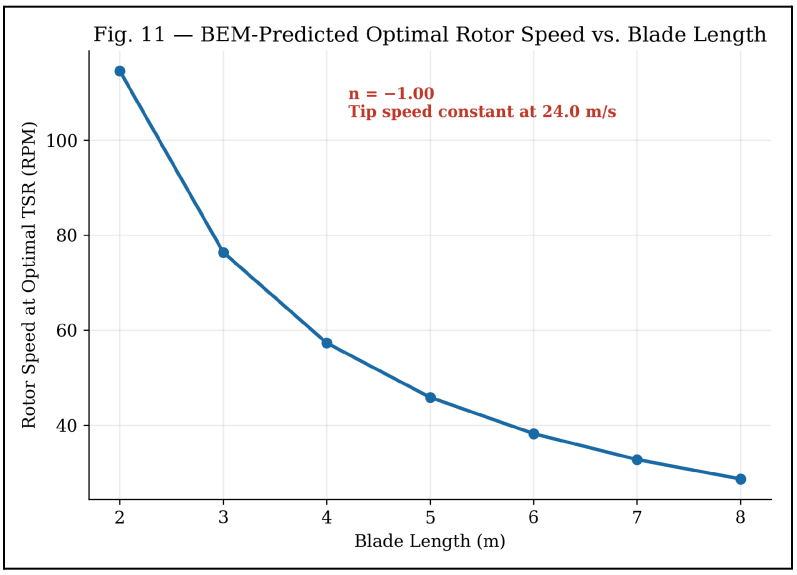



**Figure 11**. Optimal rotor rotational speed decreases with blade length at each rotor's own optimal tip-speed ratio ($\lambda \approx 2.9$).

As shown in Figure 10, rotor thrust is found to be increasing from about 384 N at R=2 m to 6,137 N at R=8 m. This is consistent with the expected $r^2$ dependence for geometrically similar rotors, with roughly constant aerodynamic coefficients, at a constant wind speed. The torque of the rotors increased from around 149 N · m to 9,566 N · m over the same range, consistent with $r^3$ dependence since the aerodynamic force and the characteristic moment arm are both proportional to rotor radius. The rotors'

corresponding rotational speed reduces by around 2.9 times, also approximately as $r^{-1}$, since they are designed to best work for the same optimum tip speed ratio. , $\lambda \approx 2.9$. The corresponding decrease in optimal rotational speed with rotor radius is shown in Figure 11.

### 3.9 Interrelationships among power, structural loading, and cost

The above-mentioned parameters of power, structure, and economy are closely interwoven. The longer a blade, the greater is the power it can capture and the greater is the rotor thrust acting on it, which raises the root bending moment, thus requiring more structural reinforcement and consequently a higher Relative Manufacturing Cost Index. The trends must be understood in the context of the current deterministic model, since the radius of the rotor is used in the aerodynamic, structural, and cost analysis in the form of predetermined mathematical relationships.

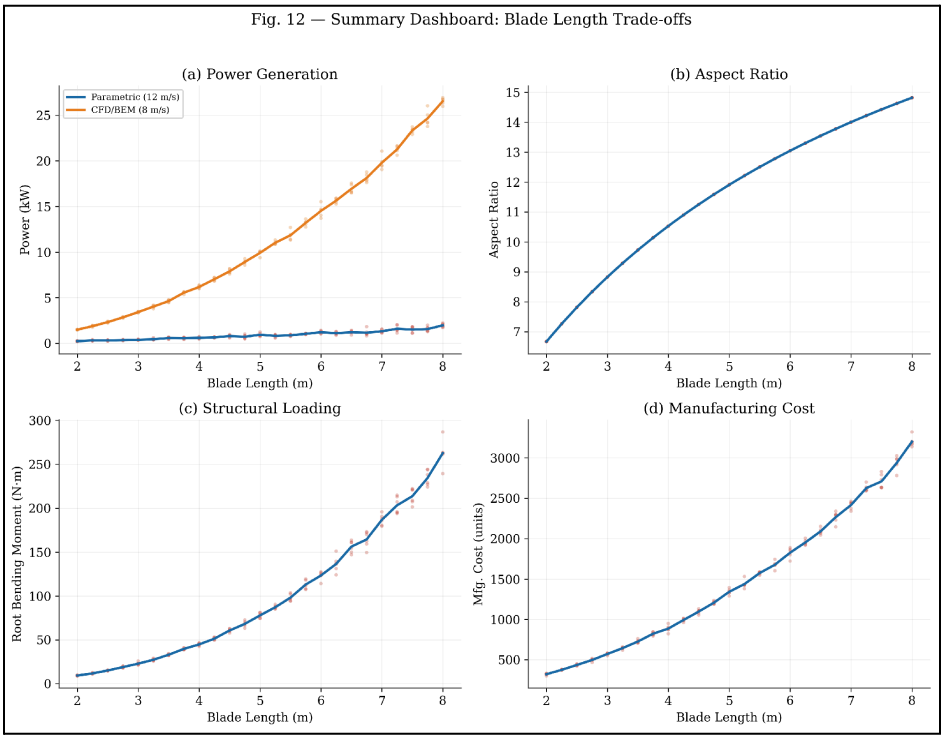



**Figure 12.** Summary comparison of aerodynamic performance, structural response and modeled Relative Manufacturing Cost Index across the investigated rotor-radius range. Structural response increases with rotor radius, but the adopted structural utilization criteria are not reached within the 2–8 m range.

The analysis directly couples the aerodynamic performance with the structural loading, as the aerodynamic forces applied to the blade are derived from the BEM solution and not from a separate prescribed loading distribution. BEM power and thrust increase strongly with rotor size over the rotor-radius range investigated, as do the root bending moments (flapwise and edgewise). The structural results, therefore, confirm that as the aerodynamic loading increases (sizing up of the rotor), the bending stress and blade deflection are increasing. Previous correlations between independently computed

parametric structural loads and BEM thrust are no longer used for demonstrating the agreement between the models, since the aerodynamic and structural calculations are tightly coupled.

The calculated responses were compared with the adopted stress and deflection screening criteria to evaluate if these responses reflect a structural limit. The maximum combined bending stress, 1.270 MPa, at the largest radius investigated (R=8 m) represents a stress utilization ratio of U=0.0127, or 1.27%. The flapwise tip deflection of 7.039 mm corresponds to a deflection utilization ratio (U) of 0.00880, or 0.88%. Both usage ratios are well below one. Thus, there was no structural limit for these structures in the radius range 2-8 m investigated because of stress or deflection.

The aerodynamic, structural, and cost trends are summarized in a single plot for the range of rotor radius considered in this study (Figure 12). Panel (a) shows a comparison between the corrected efficiency-adjusted parametric power estimate and the BEM-predicted aerodynamic rotor power. The trend of both power calculations is quadratic, but both are based on a different wind speed, different modeling assumptions and should not be compared as being run at the same operating conditions. The other panels are a summary of the corresponding aerodynamic, structural, and modeled manufacturing-cost trends. The structural response increases as the rotor radius increases, while the stress and deflection utilization criteria used are less than unity within the 2–8 m range. The present results therefore do not show a structural upper limit in the range investigated that is due to stress or deflection.

### 3.10 BEM Verification Against the NREL Phase VI Rotor

The BEM implementation was tested on a published benchmark problem from the NREL Phase VI wind tunnel with the uniform-inflow condition of 7 m/s. The verification rotor was 5.29 m in radius, with a pair of blades, a rotational speed of 72 rpm, a blade-pitch angle of 3°, published Phase VI chord and twist distribution, and the NREL S809 airfoil polar at approximately $Re = 1.0 \times 10^6$. The same 24-station BEM discretization was applied in the verification case. At this operating point, the published experiment shows a rotor power of ~6.030 kW and a rotor thrust of 1.120 kN. The present BEM implementation predicted 6.152 kW and 1.245 kN, with differences of about 2.02% in power and 11.2% in thrust. The difference between the rotor torque calculated and experimental was about 2.02% because the calculated rotor torque was 815.9 N·m and the experimental was approximately 799.8 N·m, obtained by dividing the measured rotor power by the rotational speed. The power coefficient corresponding to this was Cp=0.369 and was approximately 0.361 from the experimental power. The results show good agreement for rotor power and rotor torque and a larger difference in thrust, as expected based on the limitations of the simplified steady BEM representation.

**Table 4.** Verification of the BEM implementation against the NREL Phase VI wind-tunnel case at $U = 7$ m/s and 72 rpm.

| **Quantity** | **Experiment** | **Present BEM** | **Difference (%)** |
|---|---|---|---|
| Power (kW) | 6.030 | 6.152 | 2.02 |
| Torque (N·m) | 799.8 | 815.9 | 2.02 |
| Thrust (N) | 1,120 | 1,245 | 11.2 |
| $C_p$ | 0.361 | 0.369 | 2.02 |

## 4. DISCUSSION

The results show the scaling behaviour as predicted by the governing equations of the two models, parametric and BEM. The trends should not be taken as a stand-alone test of the models. As the blades get longer, the rotor's sweep area and effective planform increase, and more kinetic energy of the incoming wind is intercepted and extracted from it, with the BEM-predicted aerodynamic rotor power increasing approximately as $P_{aero} \propto r^2$, as in the Introduction. The Blade Element Momentum analysis predicts a maximum power coefficient $C_{p,\max}$ of approximately 0.440 at a tip-speed ratio of approximately 2.9, which remains below the Betz limit of 0.593. Across the BEM analysis, aerodynamic power increased from approximately 1.73 kW for the 2 m rotor to 27.74 kW for the 8 m rotor, corresponding to an increase by a factor of approximately 16.

The predicted optimum tip-speed ratio of $\lambda_{opt} \approx 2.9$ is relatively low compared with many conventional three-bladed, high-speed wind-turbine rotors. In the present study, this value should be interpreted as a consequence of the simplified preliminary rotor geometry and aerodynamic assumptions rather than as a universal optimum for three-bladed turbines. The blade geometry was generated using a low design tip-speed ratio of $\lambda_{design} = 2.5$ and a fixed design lift coefficient, while the BEM calculation employed a simplified Reynolds-independent polar rather than measured Reynolds-dependent airfoil data. These assumptions favor a comparatively low-speed, higher-torque operating regime. Consequently, the predicted $\lambda_{opt} \approx 2.9$ and associated torque levels are specific to the modeled rotor and should not be generalized to modern utility-scale three-bladed turbines. The Monte Carlo analysis was only employed as an exercise in uncertainty propagation for the simplified parametric power calculation. The wind-speed variability was stipulated to be normally distributed with a 6% standard deviation of the nominal wind

speed, under which condition the Monte Carlo mean power at $R = 8$ m was 81.2985 kW, which is very close to the deterministic value of 80.4399 kW. This increase is very close to the analytical value of 1.080%, which is expected for a cubic relationship with the normally-distributed wind speed. This agreement confirms that the sampling procedure is being followed, but should not be interpreted as experimental validation of the turbine model. The Monte Carlo analysis does not account for uncertainty in the BEM aerodynamic model, the turbine's structural properties, the Relative Manufacturing Cost Index, the generator behavior, or other turbine subsystems.

Unlike higher-fidelity three-dimensional CFD studies reported in the literature, the present BEM model did not predict an increase in $C_{p,\,\max}$ with blade size. It was basically the same for all seven different blade lengths in the BEM model. This is a direct result of the simplified model used, which is a non-Reynolds-number-dependent airfoil polar, while in reality, larger blades will have a higher local chord Reynolds number, which will lower viscous drag and increase the lift-to-drag ratio, which this simplified model cannot capture. This distinction is important to remember because it helps differentiate a physical property of the rotor and an aerodynamic property of the rotor from the limitations of the modelling approach, and therefore, it helps identify exactly where higher fidelity aerodynamic modelling, one dependent on the Reynolds number of the rotor, Reynolds-number-dependent airfoil polars or full three-dimensional CFD, would be most helpful (Ashuri et al. 2016; H. Aa. Madsen et al. 2011).

The aerodynamic results are not only important, but the structural analysis also shows the need for direct coupling between aerodynamic loading and the structural model. The BEM-derived sectional forces have been applied to the blade to calculate the flapwise root bending moment which was found to be 0.139 kN·m for the 2 m blade and 8.93 kN·m for the 8 m blade, and the aerodynamic edgewise root moment which was found to be 0.040 kN·m for the 2 m blade and 2.59 kN·m for the 8 m blade. The maximum combined bending stress was raised from 0.184 MPa to 1.270 MPa, and the deflection of the tip of the flapwise was raised from 0.093 mm to 7.039 mm. These values are significantly higher than those calculated based on the previously independent loading distribution and highlight the significance of aerodynamic–structural consistency. The results shown, however, are those of steady aerodynamic loading only and are not in themselves a structural design limit. The structural acceptability is assessed based on material allowables, safety factors, blade clearance and other design load cases.

## 5. CONCLUSION

The effect of blade length on the aerodynamic performance and structural response of the wind turbine was studied for rotor radii varying from 2 m to 8 m. The BEM analysis predicted the maximum power coefficient to be around 0.440 with a tip-speed ratio of around 2.9. As expected, BEM predicted aerodynamic power increased with swept area, with available rotor power rising from around 1.73 kW at 8 m/s wind speed for the 2 m rotor to 27.74 kW at 8 m/s wind speed for the 8 m rotor. The BEM sectional aerodynamic forces were directly coupled with the Euler–Bernoulli beam model. The BEM-coupled structural model resulted in the following variation in flapwise root bending moment (0.139 to 8.93 kN·m), maximum combined bending stress (0.184 to 1.270 MPa), and flapwise tip deflection (0.093 to

7.039 mm) across the 2–8 m rotor radius range. These values at the endpoints are approximately 64.2 and 75.7 times the values at the centerline. Comparing these results with the given structural criteria revealed that both the stress and deflection utilization were less than unity across the range investigated. Therefore, no stress or deflection limit was found between 2 and 8 m under the aerodynamic loading that is considered steady.

At the largest investigated rotor radius of 8 m, the stress and deflection utilization ratios were only 0.0127 and 0.00880, respectively. Hence, there was no stress- or deflection-based structural limit found for the range of 2–8 m investigated. The results show that the aerodynamic power capture and the structural demand both increase when rotor size is increased. The present simplified analysis, however, will not identify any structural failure or maximum allowable blade length since material allowables, safety factors, blade-clearance criteria, gravitational loading, centrifugal loading, and complete turbine design-load cases were not assessed.

The benchmark comparison is not an experimental validation of the geometrically scaled rotors studied in this paper, but it is an evaluation of BEM implementation with a published reference rotor configuration. Likewise, the convergence study does not quantify the model-form uncertainty resulting from the simplified airfoil polar or beam assumptions, or cost formulation.

## 6. FUTURE PERSPECTIVE

There are several ways this work could be extended and strengthened. For the first one, the airfoil polars (such as those produced by XFOIL at the local blade-station Reynolds numbers) can be used to better represent the aerodynamics. In the future, full three-dimensional CFD could be used to find the flow-field features, such as the pressure distribution, the separation and wake formation, which can not be obtained using the present BEM model. Second, the structural model used in this study is based on simplified beam theory relationships applied to a few specific reference points, and a finite element structural analysis of the root and spar (which would include real material properties and manufacturing tolerances) would greatly enhance confidence in the bending moment, stress, and tip deflection predictions. Third, the blade length and number of blades were kept constant; it may be worth investigating in future how optimal blade length varies with different wind conditions, numbers of blades and active pitch control schemes. The present study evaluated the BEM implementation against a published wind-tunnel test; however, future testing of the specific rotor geometries studied herein is recommended. Such testing would provide direct validation of the predicted aerodynamic and structural responses and would support improved quantification of model uncertainty. It would also aid in quantification of the uncertainty in the Relative Manufacturing Cost Index model, which is based on simplified scaling assumptions, instead of vendor quotes for fabrication costs.

**Conflict of interest:** There is no potential conflict of interest to disclose.

**Funding information:** There is no funding information to disclose.

**Data availability statement:** Data can be made available on reasonable and valid request.

**Code availability statement:** Code can be made available on reasonable and valid request.

**AI tool assistance:** The authors declare that no artificial intelligence (AI) tools were used in the preparation of this manuscript.

## REFERENCES

Alipour, Fatemeh, and Mohammad Reza Rahimpour. 2024. 'Components of Wind Turbines (Rotors, Blades, Drive Trains, Gearboxes, Generators, Etc.)'. *Encyclopedia of Renewable Energy, Sustainability and the Environment*, 343–60. https://doi.org/10.1016/b978-0-323-93940-9.00228-0.

Andrew Ning, S. 2013. 'A Simple Solution Method for the Blade Element Momentum Equations With Guaranteed Convergence'. *Wind Energy*, June 17, n/a–n/a. https://doi.org/10.1002/we.1636.

Ashuri, Turaj, Michiel B. Zaaijer, Joaquim R. R. A. Martins, and Jie Zhang. 2016. 'Multidisciplinary Design Optimization of Large Wind Turbines—Technical, Economic, and Design Challenges'. *Energy Conversion and Management* 123 (September): 56–70. https://doi.org/10.1016/j.enconman.2016.06.004.

Betz, A. 2013. 'The Maximum of the Theoretically Possible Exploitation of Wind by Means of a Wind Motor'. *Wind Engineering* 37 (4): 441–46. https://doi.org/10.1260/0309-524x.37.4.441.

Biswas, Saroj, and Jim Shih-Jiun Chen. 2025. 'Power Coefficient for Large Wind Turbines Considering Wind Gradient Along Height'. *Energies* 18 (3): 740. https://doi.org/10.3390/en18030740.

Burton, Tony, Nick Jenkins, David Sharpe, and Ervin Bossanyi. 2011. *Wind Energy Handbook*. John Wiley & Sons, Ltd. https://onlinelibrary.wiley.com/doi/book/10.1002/9781119992714.

Canet, Helena, Pietro Bortolotti, and Carlo L. Bottasso. 2021. 'On the Scaling of Wind Turbine Rotors'. *Wind Energy Science* 6 (3): 601–26. https://doi.org/10.5194/wes-6-601-2021.

Cardoza, Adam, and Andrew Ning. 2026. 'Efficient Derivative Computation for Unsteady Fatigue-Constrained Nonlinear Aero-Structural Wind Turbine Blade Optimization'. *Wind Energy Science* 11 (4): 1487–504. https://doi.org/10.5194/wes-11-1487-2026.

Firoozi, Ali Akbar, Farzad Hejazi, and Ali Asghar Firoozi. 2024. 'Advancing Wind Energy Efficiency: A Systematic Review of Aerodynamic Optimization in Wind Turbine Blade Design'. *Energies* 17 (12): 2919. https://doi.org/10.3390/en17122919.

Hu, Weifei, Dohyun Park, and DongHoon Choi. 2013. 'Structural Optimization Procedure of a Composite Wind Turbine Blade for Reducing Both Material Cost and Blade Weight'. *Engineering Optimization* 45 (12): 1469–87. https://doi.org/10.1080/0305215x.2012.743533.

Ingersoll, Bryce, and Andrew Ning. 2020. 'Efficient Incorporation of Fatigue Damage Constraints in Wind Turbine Blade Optimization'. *Wind Energy* 23 (4): 1063–76. https://doi.org/10.1002/we.2473.

Kelele, Hailay, Lars Frøyd, Mulu Kahsay, and Torbjørn Nielsen. 2022. 'Characterization of Aerodynamics of Small Wind Turbine Blade for Enhanced Performance and Low Cost of Energy'. *Energies* 15 (21): 8111. https://doi.org/10.3390/en15218111.

Le, Dang Huy, The Bao Nguyen, and Van Minh Ngo. 2025. 'Application of Blade Element Momentum Theory With Guaranteed Convergence to Analyze a Straight-Blade Horizontal Axis Wind Turbine'. *International Journal of Air-Conditioning and Refrigeration* 33 (1). https://doi.org/10.1007/s44189-025-00078-y.

Madsen, H. Aa., V. Riziotis, F. Zahle, et al. 2011. 'Blade Element Momentum Modeling of Inflow With Shear in Comparison With Advanced Model Results'. *Wind Energy* 15 (1): 63–81. https://doi.org/10.1002/we.493.

Madsen, Helge Aa., Christian Bak, Mads Døssing, Robert Mikkelsen, and Stig Øye. 2009. 'Validation and Modification of the Blade Element Momentum Theory Based on Comparisons With Actuator Disc Simulations'. *Wind Energy* 13 (4): 373–89. https://doi.org/10.1002/we.359.

Manwell, J. F., J. G. McGowan, and A. L. Rogers. 2009. *Wind Energy Explained*. John Wiley & Sons, Ltd. https://onlinelibrary.wiley.com/doi/book/10.1002/9781119994367.

Mehta, Mihir Kishore, Michiel Bastiaan Zaaijer, and Dominic von Terzi. 2023. *Turbine Scaling for Offshore Wind Farms*. May 5. https://doi.org/10.5194/wes-2023-39.

Okulov, Valery L., and Gijs A. M. van Kuik. 2009. 'The Betz-Joukowsky Limit for the Maximum Power Coefficient of Wind Turbines'. *International Scientific Journal for Alternative Energy and Ecology* 9 (9): 106–11.

Shen, Wen Zhong, Robert Mikkelsen, Jens Nørkær Sørensen, and Christian Bak. 2005. 'Tip Loss Corrections for Wind Turbine Computations'. *Wind Energy* 8 (4): 457–75. https://doi.org/10.1002/we.153.

Zhong, Wei, Tongguang Wang, Wen Zhong Shen, and Wei Jun Zhu. 2024. 'A Function Improving Tip Loss Correction of Blade-Element Momentum Theory for Wind Turbines'. *International Journal of Sustainable Energy* 43 (1). https://doi.org/10.1080/14786451.2024.2352794.

Öchsner, Andreas. 2021. 'Euler–Bernoulli Beam Theory'. *Classical Beam Theories of Structural Mechanics*, 7–66. https://doi.org/10.1007/978-3-030-76035-9_2.